Spectroscopy of nanoantenna-covered Cu₂O: Towards enhancing quadrupole transitions in Rydberg excitons

Annika Neubauer [1], Julian Heckötter [2], Monika Ubl [1], Mario Hentschel [1], Binodbihari Panda [2], Marc Aßmann [2], Manfred Bayer [2], and Harald Giessen [1,*]

[1]*4th Physics Institute and Research Center SCoPE, University of Stuttgart, Pfaffenwaldring 57, D-70569 Stuttgart, Germany*
[2]*Experimentelle Physik 2, Technical University Dortmund, Otto-Hahn-Straße 4a, D-44227 Dortmund, Germany*

Plasmonic antennas channel incoming light into a confined near field that comes along with strong field gradients at the edges. Transverse field gradients are capable of driving quadrupole transitions in a more effective way than the weak longitudinal field gradient in dipolar light. Cuprous oxide Rydberg excitons with principal quantum number n between 5 and 15 are several tens to a few hundreds of nanometers in diameter and can have different orbital angular momentum quantum numbers. Usually, only P- and F-excitons are electric dipole allowed, while S- and D-excitons remain dark. Here, we use 30-nm-wide and 60- to 110-nm-long plasmonic aluminum nanoantennas deposited on the cuprous oxide crystal surface to create transverse field gradients in similar spatial dimensions as the size of the Rydberg excitons. This way, light field and matter wave function overlap spatially and quadrupole transitions of S excitons are enhanced. The relative enhancement of the S-exciton oscillator strength with respect to the P-exciton oscillator accounts for a factor of up to 1.4.

I. INTRODUCTION AND MOTIVATION

Semiconductors have stimulated intense research interest both in fundamental and applied physics. An exciton is an elemental excitation in a semiconductor, which can be considered as hydrogen-like bound state of an electron and a hole. Excitons were theoretically proposed by Frenkel in 1931 [1] and Wannier in 1937 [2], and experimentally found in cuprous oxide in 1950 by Hayashi and Katsuki [3] and in 1952 by Gross and Karryjew [4]. In the 1970s and 1980s intensive research was performed on excitons in cuprous oxide in the form of modulation spectroscopy [5], forbidden resonant Raman scattering [6], and high-pressure x-ray studies [7,8]. Cuprous oxide has in total ten valence and four conduction bands with a direct band gap of $E_g = 2.17$ eV [see Fig. 1(c).] Since conduction and valence bands have the same (positive) parity, direct dipole transitions are forbidden and the radiative lifetimes of the excitons are relatively large. The exciton fine structure was investigated experimentally by applying external fields [9]. The even-parity [10] as well as odd-parity [11] excitons were identified, and in 1981 Uihlein succeeded with a first complete theoretical description of S- and D-excitons for up to $n = 5$. The research continued into the 1990s with a detailed investigation of the exciton fine structure [12], where it was found that the coupling of electron and hole to LO phonons produces a frequency dependence of the dielectric function $\varepsilon(k, \omega)$. In 1996 Matsumoto probed S- and D-excitons up to $n = 7$ in two-photon experiments [13].

In 2014 P-excitons were probed up to principal quantum numbers as large as $n = 25$ in transmission measurements [14], which renewed the research interest in Rydberg excitons in cuprous oxide [15]. Further transmission [16] and photoluminescence emission [17] measurements found Rydberg excitons with principal quantum numbers up to $n = 30$. These highly excited excitons are similar to Rydberg atoms with the advantage of being embedded in the semiconductor. This allows for straightforward integration into a more complex solid-state system. Starting from this system, one can demonstrate schemes that harness light–Rydberg-exciton interaction, as well as study Rydberg-Rydberg interactions. Furthermore, having macroscopic quantum objects (Bohr radii of up to micrometer size) is advantageous for integrated and scalable solid-state quantum devices [18]. The wavelength of light is on the same order of magnitude as the Rydberg exciton wave-function diameter. This allows for good overlap and is crucial for a strong interaction. In the last couple of years intensive research has been conducted in order to identify similarities or differences between Rydberg excitons and Rydberg atoms, i.e., Rydberg blockade [14,19], quantum defect [20,21], higher angular momentum states [22], Rydberg excitons in external fields [23,24], and quantum-coherent effects among Rydberg excitons [25]. Much theoretical work was done on the electro- and magneto-optical properties of Rydberg excitons [26–28]. Focus was also placed on solid-state specific effects, such as phonon-assisted absorption [29] and interactions with the electron-hole plasma [30,31]. Two-photon absorption and second-harmonic generation were used to probe the dipole-forbidden even-parity excitons up to $n = 12$ [32–34], and detailed theoretical calculations were performed [35,36]. Rydberg excitons trapped in potential [37,38] and quantum [39] wells, as well as in microcrystals [40] were studied. Lately, the research on Rydberg excitons in cuprous oxide has been extended to excitation by orbital angular momentum light [41], and, charged impurities [16,42] have been found to be the limiting factor for the existence of
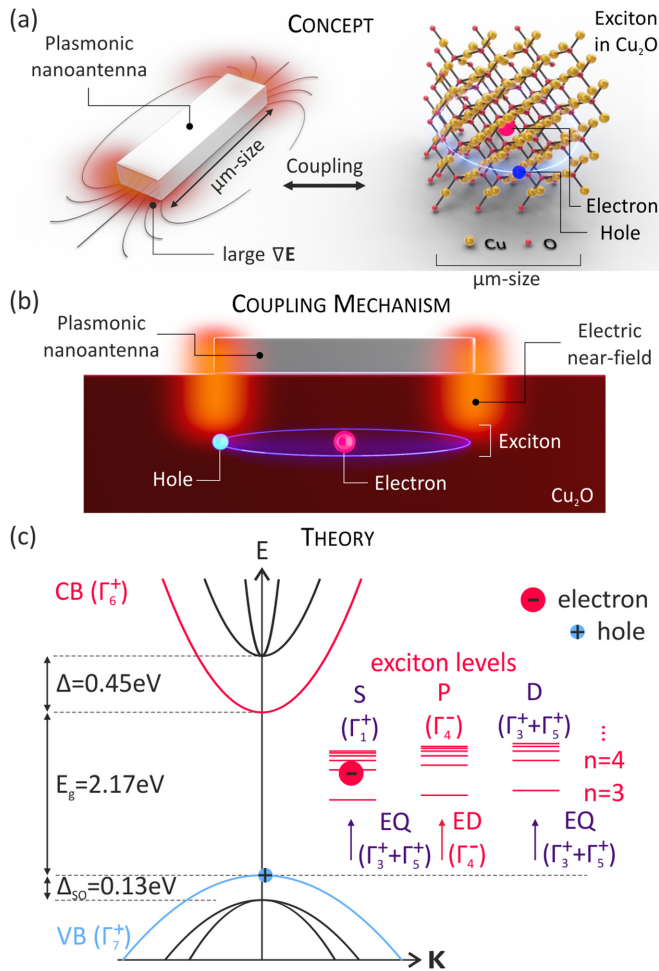
FIG. 1. (a) Concept of coupling a plasmonic nanoantenna to Rydberg excitons in cuprous oxide. Strong inhomogeneous E fields result in strong gradients $\nabla\mathbf{E}$, allowing for enhanced quadrupole transitions, favored by matching sizes of light field and Rydberg exciton. (b) Illustration of the coupling mechanism between a plasmonic nanoantenna and a Rydberg exciton. Strong field gradients at the antenna tips are expected to strongly interact with the Rydberg excitons when brought in close proximity. (c) Schematic drawing of the dispersion relation of cuprous oxide at the Γ point, explaining the coupling theoretically. Energy gap (E_g), as well as crystal field (Δ) and spin-orbit (Δ_SO) splitting, are indicated. The symmetries of conduction- (CB) and valence (VB) bands of S-, P-, and D-exciton levels, as well as of the corresponding light field operators (electric dipole ED / electric quadrupole EQ) are shown.

high principal quantum number excitons with $n \geqslant 25$. Very recently, Rydberg exciton-polaritons in a Cu$_2$O microcavity were investigated [43].

The research on Rydberg excitons in cuprous oxide is of great interest as they can be utilized for establishing solid-state quantum technologies. In particular, addressing a variety of angular momentum exciton states is interesting for quantum information processing [44]. In this paper, we want to excite even angular momentum exciton states, and, in particular enhance quadrupole transitions of Rydberg excitons with the use of plasmonic nanoantennas. The concept of the related problem for the $1S$-exciton in cuprous oxide has already been

proposed theoretically [45]. Concept and proposed coupling mechanism are sketched in Figs. 1(a) and 1(b). Plasmonic nanoantennas exhibit a strong field enhancement at their tips when illuminated with resonant light. Strong field gradients extend over a range of a few to a few tens of nanometers. When brought in close proximity to Cu$_2$O Rydberg excitons, we expect strong interaction of the gradient light fields with the excitonic transitions due to their matching size [46].

II. THEORY

In order to derive how the electric quadrupole of the excitonic transition interacts with an external field, we start from the multipole expansion of the energy of a localized charge distribution $\rho(\mathbf{x})$ placed in an external potential $\Phi(\mathbf{x})$ [47]. The electrostatic energy of the system reads

$$W = \int \rho(\mathbf{x})\,\Phi(\mathbf{x})d^3x. \qquad (1)$$

After expanding the potential into a Taylor series and using the definition of the electric field $\mathbf{E} = -\nabla\Phi$, with $\nabla \cdot \mathbf{E} = 0$ for the external field, Eq. (1) can be approximated as

$$W = q\Phi(0) - \mathbf{p} \cdot \mathbf{E}(0) - \frac{1}{6}\sum_i\sum_j Q_{ij}\frac{\partial E_j}{\partial x_i}(0), \quad \text{Ref. [48]} \qquad (2)$$

with total charge q, dipole moment $\mathbf{p}$, and quadrupole moment Q_{ij}, while higher multipole terms have been omitted [48]. From Eq. (2) one sees that the quadrupole interacts with the field gradient $\nabla\mathbf{E}$.

Electric quadrupole transitions caused by the longitudinal field gradient of a light field are usually three orders of magnitude weaker than the electric dipole transition. On the other hand, the transverse field gradient in orbital angular momentum light causes enhanced quadrupole transitions [49–53]. Plasmonic antennas have the property of channeling incoming electromagnetic energy into a confined near field. This results in a strongly inhomogeneous field distribution, and comes with strong transverse field gradients at the edges of the antenna that are capable of driving quadrupole transitions.

Whether an optical transition is forbidden or allowed is determined by the selection rules. This can also be predicted by symmetry considerations of the initial and final state of the quantum object as well as the light field operator. The symmetries of Rydberg excitons in cuprous oxide Γ_exc are composed of the cuprous oxide valence- and conduction-band symmetries, Γ_V and Γ_C, respectively, as well as the exciton envelope symmetry Γ_env^l, determined by the angular momentum quantum state:

$$\Gamma_\mathrm{exc} = \Gamma_V \,\otimes\, \Gamma_C \,\otimes\, \Gamma_\mathrm{env}^l. \qquad (3)$$

Conduction- and valence-band symmetries are known from literature [54]. The exciton envelope functions are described by spherical harmonics and can be assigned to a symmetry operator with the help of the tables by Koster *et al.* [55] [see Fig. 1(c)]. For allowed transitions, the overlap of crystal ground- (Γ_1^+) and excited (Γ_exc) states contains the symmetry of the light field operator (Γ_Q). A multiplication with Γ_1^+ leaves the symmetry unchanged. The quadrupole operator, having symmetry $\Gamma_Q = \Gamma_3^+ \oplus \Gamma_5^+$, thus allows for a nonzero transition probability of S- and D-excitons with symmetries

TABLE I. Overview over different plasmonic antenna dimensions and the spectral position of their plasmonic resonance.

| Name | Length (nm)×Width (nm) | | Resonance (nm) |
	Designed	Measured	
F1	110×30	115×40	>600
F2	90×30	95×40	600
F3	80×30	85×35	575
F4	70×30	75×35	550
F5	60×30	65×35	525

$\Gamma_S = \Gamma_2^+ \oplus \Gamma_5^+$ and $\Gamma_D = \Gamma_1^+ \oplus 2\Gamma_3^+ \oplus 3\Gamma_4^+ \oplus \Gamma_5^+$, respectively. The overlap is given by the symmetry operator Γ_5^+.

In addition, the size of the Rydberg excitons is comparable to the plasmonic antenna, and, thus, the field gradient extension. This implies a strong interaction of the Rydberg exciton with the confined optical light field and should lead to an additional enhancement of the quadrupole transitions.

III. EXPERIMENT

Plasmonic nanoantennas can be directly fabricated on the cuprite crystal surface using electron-beam lithography. The antennas used are made of aluminum and are designed to be 30 nm wide and 60 to 110 nm long (see Table I) in order to exhibit plasmon resonances along the long axis at the exciton energies around 2.17 eV or 571 nm. By varying the antenna length, the plasmon resonance can be tuned (see Fig. 2), and by changing the laser polarization the plasmon resonance can be switched on and off. An in-house implementation of a numerical Maxwell solver based on the Fourier modal method is used in order to simulate the antenna response and, thus, to design the antenna [56,57]. We use antenna arrays with periodicity of 160 nm. Large antenna arrays of $200 \times 200\,\mu$m^2 are fabricated onto the polished cuprite surface to guarantee optical access in the experiment. This way, the surface becomes equipped with a large number of field gradients when being illuminated with a focused light beam. Under ideal conditions the nanoantenna geometry we employed may result in a field enhancement factor of 10 [58,59]. The field gradient enhancement, however, is difficult to determine.

The nanoantennas are fabricated onto the polished cuprous oxide surface with standard electron-beam lithography (Raith eLINE Plus). The bare cuprite sample is cleaned in an ultrasonic bath with acetone and propanol. The sample is glued onto a glass substrate using resin with $T_{\text{melt}} = 60°$ C (Struers GmbH). The positive, high-resolution photoresist AR-P 6200 (CSAR 62, Allresist) is spin coated onto the sample. The antenna arrays are defined and written by electron-beam exposure at 20 kV and an area dose of $65\,\mu$m/cm^2. At the exposed areas the photoresist chains break up so they become dissolvable in the developer. After development, an adhesive layer of 2 nm titanium and 20 nm aluminum are consecutively evaporated using an electron gun evaporator. A lift-off process is started with a commercial n-ethyl-2-pyrrolidon–based remover (Allresist) at 60 °C. Afterwards the structured cuprite flake is cleaned with acetone and propanol. The different
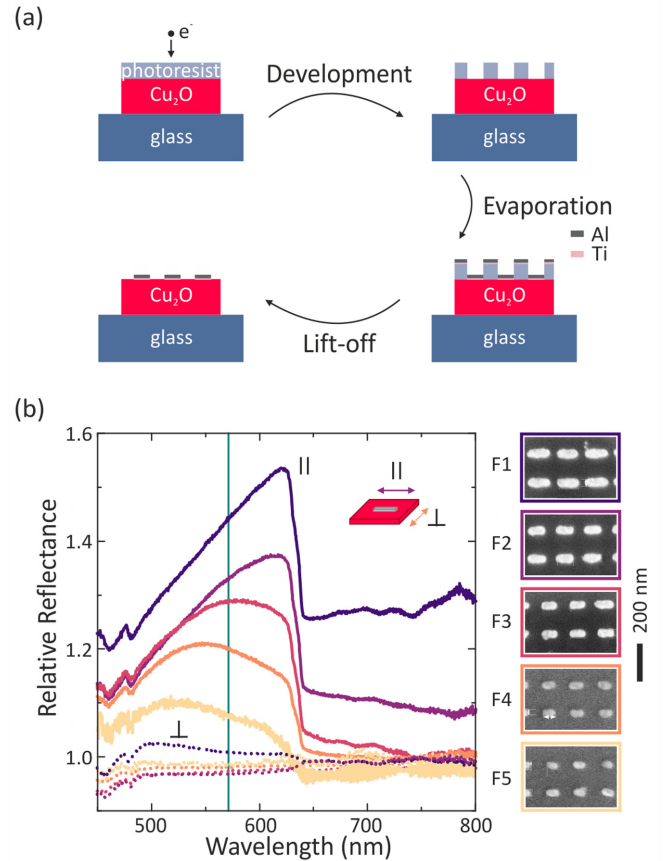
FIG. 2. (a) Scheme of single-layer electron-beam lithography. The main steps are electron-beam exposure of the poly(methyl methacrylate) (PMMA) photoresist, development, evaporation of an adhesive titanium (Ti) layer followed by aluminum (Al), and lift-off. Figure based on Ref. [60]. (b) Measured plasmon resonances of antenna fields F1–F5 together with their scanning electron microscope images. The plasmon resonances are active for light at energies around the exciton resonance at 571 nm (vertical green line) that is parallel ($\parallel$) polarized to the long antenna axis. Relative reflectance is the ratio between reflectance measurements on the antenna fields over measurements on the Cu$_2$O surface without antennas.

fabrication steps are visualized in Fig. 2(a). For more details about the fabrication process see Ref. [60].

The cuprous oxide crystals used are high-quality natural crystals from the Tsumeb mine in Namibia. They were polished to a thickness of 46 μm (sample 1) and 104 μm (sample 2), respectively. The plasmonic antenna fields are imprinted on the crystal front facet, which is {110} oriented. Experiments are performed in reflection geometry with 15° angle of incidence. Due to the small thickness of sample 1, reflection as well as transmission spectroscopy is performed. The probe laser is a tunable dye laser with spot diameter of 100 μm and laser power of 6 μW. The probe laser is scanned from $\lambda = 574.67$ to $\lambda = 570.84$ nm (2.1575–2.17195 eV) and from $\lambda = 572.01$ to $\lambda = 571.42$ nm (2.1675–2.16975 eV) for a detailed look into the $n = 5$ excitons. A reference signal is recorded in order to compensate for the laser interferences appearing in the reflection signal. Sample 2 is investigated using pump-probe spectroscopy in reflection geometry. As light

sources, two solid-state lasers are used. The probe laser spot diameter is 150 μm and the probe power is 40 μW. The pump power at $\lambda = 561$ nm is 3 mW. The probe laser is scanned from $\lambda = 571.60$ to $\lambda = 571.40$ nm (2.1691–2.1698 eV) for investigating the $n = 6$ excitons.

For constant laser intensity, the light beams are stabilized by a BEOC laser power controller (LPC by Brockton Electro-Optics Corp.). The combination of a slightly tilted half-wave plate and a Glan-Taylor prism allows for further attenuation of the laser light without interferences. The collimated signals are detected via photodiodes with variable gain (New Focus Large-Area Photoreceiver), which are read out by high-speed multimeters (Keithley 2000) connected to a computer. For pump-probe measurements a lock-in amplifier is interconnected between photodiode and multimeter.

IV. RESULTS

The antenna resonances were measured using bright-field reflection microscopy [see Fig. 2(b)]. Under optical excitation in parallel ($\parallel$) polarization configuration, the plasmon resonance is active along the long antenna axis, while no plasmon resonance appears for perpendicular ($\perp$) polarization. The plasmon resonances are very broad (>100 nm) with their peak shifting across the exciton resonance at 571 nm. While antenna field F1 has a plasmon resonance with maximum above 600 nm, antenna field F5 has the maximum at 525 nm. The antenna field reflectance is normalized to the reflectance of the bare cuprous oxide, so the displayed values are larger than 1. The corresponding scanning electron microscope images of the different antenna fields in Fig. 2(b) illustrate that the overall reflectivity is largest on field F1 with the largest antennas. The antennas in field F5 are the smallest, so its overall reflectivity is weakest.

The cuprous oxide samples used are of good quality, which is indicated by the transmitted and reflected intensity shown in the spectra of a reference point (no antenna field) on sample 1 in Fig. 3, where Rydberg excitons with principal quantum numbers up to $n = 21$ are observed in parallel laser polarization configuration.

The top row in Fig. 4 shows the reflected signal from the antenna field F5 on sample 1 in perpendicular and parallel laser polarization configuration for $n = 5$ (left) and $n = 6$ (right) separately. The optical density data of the different polarization configurations have been shifted in the y direction for a better comparison. This does not change any physical content. For parallel laser polarization, $5S$- and $6S$-excitons appear on the low-energy P-exciton shoulder, while they are much less pronounced in perpendicular laser polarization. In order to highlight the antenna effect, $5S$- and $6S$-excitons have been fitted with a Lorentzian function S_n of the shape

$$S_n = C_n \frac{G_n/2}{(G_n/2)^2 + (x - E_n)^2},　(4)$$

with principal quantum number n, oscillator strength C_n, damping constant G_n, and energy E_n. P-excitons have been fitted with an asymmetric Lorentzian function P_n:

$$P_n = C_n \frac{(G_n/2) + 2q_n(x - E_n)}{(G_n/2)^2 + (x - E_n)^2},　(5)$$
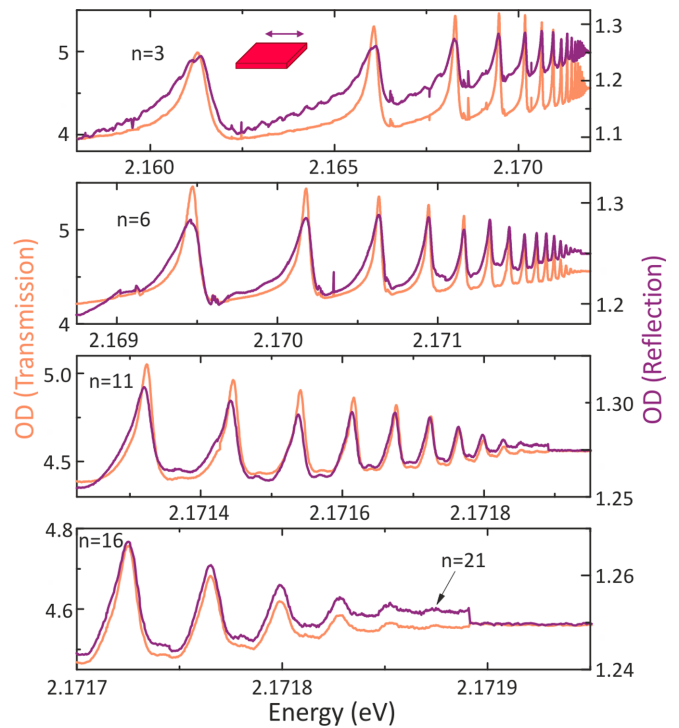
FIG. 3. Optical density (OD) of transmitted and reflected signal on a reference point (no antenna field) on sample 1. Spectra show that the crystal is of good quality, revealing Rydberg excitons with principal quantum numbers up to $n = 21$. The reflected signal is much weaker than the transmitted signal and exciton lines are broader with a flatter slope on the low-energy side.

with an additional asymmetry parameter q_n, which amounts to $q_5 = -0.35$ and $q_6 = -0.33$ for the $5P$- and $6P$-exciton, respectively. All other fit parameters are listed in Table II. The difference of the fits for parallel and perpendicular data are displayed in the middle row in Fig. 4. Despite a feature that accounts for the different P-exciton parameters in parallel and perpendicular measurements, the S-exciton, which appears stronger in parallel polarization, is clearly visible. The bottom row in Fig. 4 shows the same data as in the top row but for a reference point (no antenna field). Here, no prominent S-excitons appear in parallel laser polarization configuration.

Pump-probe spectroscopy in reflection geometry on $n = 6$ excitons also reveals that in parallel laser polarization the $6S$-exciton clearly appears on different antenna fields, while it is absent in the reference measurement (see Fig. 5). In addition, the lock-in signal decreases from the top towards the bottom graph in Fig. 5, i.e., from the longest (F1) towards the shortest (F4) antenna. As the periodicity between the antennas is kept constant for all fields, the overall reflectivity decreases from F1 towards F4.

V. DISCUSSION

For investigating Rydberg excitons in cuprous oxide, samples of good quality are essential. Furthermore, the implementation of spectroscopy experiments in reflection geometry on cuprous oxide is not straightforward. The spectra in Fig. 3 indicate that both prerequisites have been successfully ful-
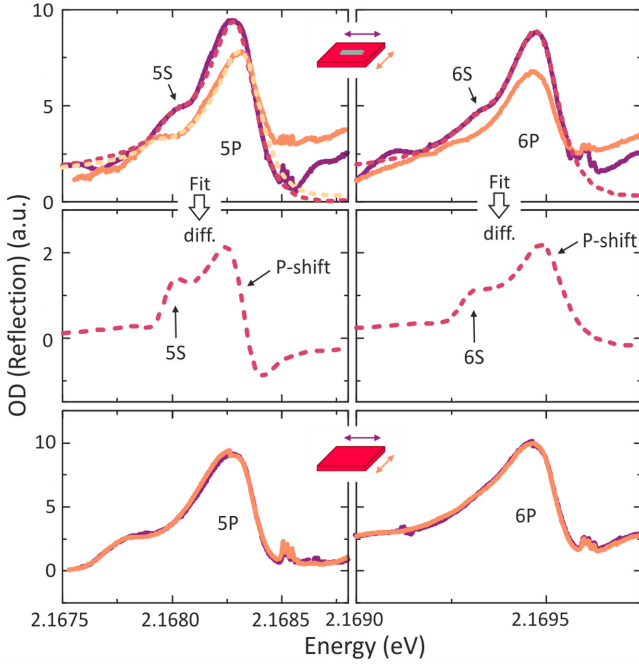
FIG. 4. Top row: Comparison of the reflected signal in parallel and perpendicular laser polarization on antenna field F5 on sample 1. On the left P-exciton shoulder, $5S$- and $6S$-excitons appear in parallel laser polarization configuration, while they are much less pronounced in perpendicular laser polarization. Middle row: Fit difference of parallel and perpendicular data. Bottom row: Same data as in top row but for a reference (no antenna field). Here, no prominent S-excitons appear in parallel laser polarization configuration.

filled. Rydberg excitons with principal quantum number up to $n = 21$ detected in the transmitted- as well as the reflected signal. The reflected signal is much weaker than the transmitted one. Here, noise and, in particular, interferences from optical elements manifest themselves to a larger extent. Therefore, the reflected signal has been divided by a reference

TABLE II. Fit parameters of $5P$-, $5S$-, $6P$-, and $6S$-excitons for measurements with polarization parallel ($\parallel$) and perpendicular ($\perp$) to the long nanoantennas axis. A Lorentzian line shape has been fitted to the S-excitons, while an asymmetric Lorentzian has been fitted to the P-excitons. Energy positions are given as $2.168\,\mathrm{eV} + \Delta_E$. $(C_S^\parallel/C_P^\parallel)/(C_S^\perp/C_P^\perp)$ denotes the enhancement factor of the relative S-to-P-oscillator strength from parallel to perpendicular measurement.

Parameter	5P ($\parallel$)	5S ($\parallel$)	5P ($\perp$)	5S ($\perp$)	6P ($\parallel$)	6S ($\parallel$)	6P ($\perp$)	6S ($\perp$)
C (10^{-7})	99	6.2	80	3.5	57	4.0	42	2.5
G (10^{-4})	2.6	1.4	2.6	1.4	1.6	1.2	1.6	1.2
Δ_E (meV)	0.32	0.00	0.50	−0.08	1.5	1.3	1.49	1.295
C_S/C_P (10^{-3})	0.062 63		0.043 75		0.070 17		0.059 52	
$\frac{C_S^\parallel/C_P^\parallel}{C_S^\perp/C_P^\perp}$	1.42				1.18			
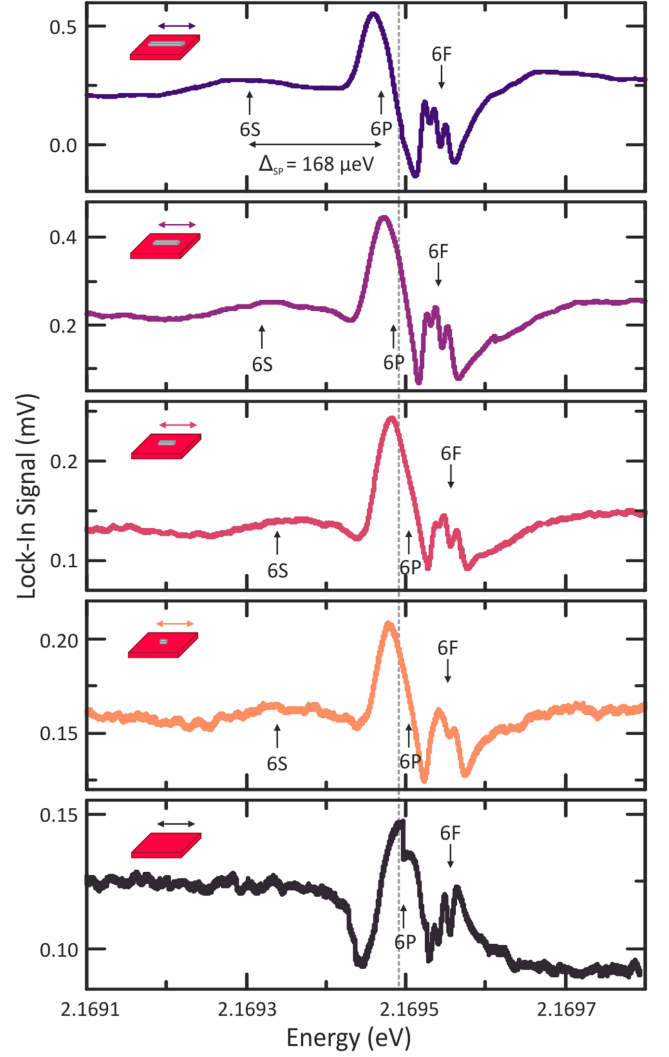
FIG. 5. Pump-probe spectroscopy data of $n = 6$ excitons on different antenna fields (F1–F4) and a reference (bottom) on sample 2 for parallel laser polarization. The $6S$-exciton appears on all antenna fields, while it is absent in the reference. A fixed $6P$-exciton energy is indicated at 2.169 49 eV by the gray dashed line.

signal. This way, most of the oscillations can be removed. In both transmitted and reflected signals we can distinguish P- and F-excitons well. The P-exciton line shapes in the reflected signal are broader and more triangular shaped compared to the ones in the transmitted signal. This behavior agrees with what has been reported in literature [61].

The peak-to-peak energy differences between S- and P-excitons in Fig. 4 are $\Delta_{SP}^{n=5} = 250\,\mu\mathrm{eV}$ and $\Delta_{SP}^{n=6} = 150\,\mu\mathrm{eV}$, while the differences of energy positions of the fitted oscillators are $\Delta_{SP,\,\mathrm{fit}}^{n=5} = 320\,\mu\mathrm{eV}$ and $\Delta_{SP,\,\mathrm{fit}}^{n=6} = 200\,\mu\mathrm{eV}$, respectively. These values agree well with literature [62] ($\Delta_{SP,\,lit}^{n=5} = 270\,\mu\mathrm{eV}$ and $\Delta_{SP,\,lit}^{n=6} = 168\,\mu\mathrm{eV}$). For the P- and S-exciton fits, respectively, we use the same damping constant G_n for results from parallel and perpendicular measurements. This allows for a comparison of the oscillator strength ratio C_S/C_P. We find an increase of this relative S-exciton oscillator strength with respect to the P-exciton oscillator strength of 1.42 and 1.18 for $n = 5$ and $n = 6$, respectively (see Table II).

One might also attribute the observed enhancement of the dipole-forbidden *S*-exciton to strain or local Schottky electric fields originating from the antennas. However, this effect would also occur in perpendicular polarization, which is not the case. Furthermore, these effects should be independent of the antenna detuning.

For certain crystal orientations, as for the one of the investigated samples ({110}), the quadrupole transition of the *S*-exciton is *per se* forbidden in one polarization configuration while it is allowed in the perpendicular polarization configuration. This can be determined by group-theoretical calculations with the help of the tables by Koster *et al.* [55]. The reference measurement in the lower panel of Fig. 4 indicates that this effect is not visible in the chosen polarization configurations. Here, for both parallel and perpendicular laser polarization no *S*-exciton appears. This confirms that the effect seen in the upper panel is most likely due to the quadrupole enhancement caused by the plasmonic antennas.

Figure 5 depicts the appearance of the 6*S*-exciton on different antenna fields F1–F4 for parallel laser polarization in comparison to a reference measurement. Clearly, the reference signal shows no 6*S*-exciton for parallel laser polarization, while on the antenna fields the 6*S*-exciton appears. The signal strength continuously increases compared to the reference via the antenna fields F4, F3, and F2, towards field F1. Here, the overall reflectivity of the sample plays a crucial role. On antenna field F1, the antennas are longest. As the periodicity is kept constant for all antenna fields, more aluminum covers the cuprous oxide, so the overall reflectivity is highest.

VI. SUMMARY AND OUTLOOK

We have demonstrated that plasmonic nanoantennas provide an apparent increase of the oscillator strength of the *S*-exciton in different measurements. However, the enhancement has turned out to be weaker than what one might have expected. The plasmonic field enhancement accounts for a factor of 10. The field gradient enhancement, however, is hard to quantify. The observed effect for the Rydberg excitons in cuprous oxide is smaller than this ideal value. Most probably

the Rydberg-exciton–antenna coupling is not fully optimized yet. Furthermore, the plasmonic antennas might create surface charges that partly screen the Coulomb interaction [63] or broaden the lines [64], which would lead to a suppression of exciton resonances. Another reason for the weak signal of plasmonic enhancement might stem from the fact that the measured signals are overlaid by absorption features not coming from the surface close to the antennas, but from the rest of the bulk sample. Simulations should help to unravel the influence of the different factors.

In order to increase the quadrupole enhancement caused by plasmonic antennas with respect to Rydberg excitons, several approaches could be used. First, the coupling between antenna and Rydberg excitons can be enhanced by localizing the Rydberg excitons very close to the antennas. Second, one can polish the crystal to ultrathin flakes with thickness below 10 μm and measure in transmission configuration. The transmitted signal is easier to interpret but will contain a significant amount of dipolar excited *P*-excitons. This amount will, however, be reduced in comparison to our current measurements by a factor of 10, so the antenna contribution gains more weight in the transmitted signal. Third, one could measure cuprite microcrystals [40] scattered among plasmonic nanoantennas. This way, the antenna field would cover the entire microcrystal. However, border effects may play a role. Nevertheless, the implementation of reflection measurements in pure reflection and pump-probe geometry is a first step towards quantum integrated fiber-detection schemes with Rydberg excitons.

[1] J. Frenkel, On the transformation of light into heat in solids, I, Phys. Rev. **37**, 17 (1931).

[2] G. H. Wannier, The structure of electronic excitation levels in insulating crystals, Phys. Rev. **52**, 191 (1937).

[3] M. Hayashi, Absorption spectra of cuprous oxide, Prog. Theor. Phys. **12**, 160 (1959).

[4] E. F. Gross, Optical spectrum of excitons in the crystal lattice, Suppl. Nuovo Vim. **3**, 672 (1956).

[5] J. C. Merle, C. Wecker, A. Daunois, J. L. Deiss, and S. Nikitine, Modulated excitonic absorption on Cu$_2$O in magnetic or parallel electric and magnetic fields, Surf. Sci. **37**, 347 (1973).

[6] M. A. Washington, A. Z. Genack, H. Z. Cummins, R. H. Bruce, A. Compaan, and R. A. Froman, Spectroscopy of excited yellow exciton states in Cu$_2$O by forbidden resonant Raman scattering, Phys. Rev. B **15**, 2145 (1977).

[7] S. Nikitine, J. B. Grun, and M. Sieskind, Etude spectrophotometrique de la serie jaune de Cu$_2$O aux basses temperatures, J. Phys. Chem. Solids **17**, 292 (1961).

[8] A. Werner and A. D. Hochheimer, High-pressure x-ray study of Cu$_2$O and Ag$_2$O, Phys. Rev. B **25**, 5929 (1982).

[9] V. T. Agekyan, B. S. Monozon, and I. P. Shiryapov, The fine structure of Wannier-Mott excitons in a cubic crystal and its behaviour in an electric field, Phys. Status Solidi B **66**, 359 (1974).

[10] D. Fröhlich, R. Kenklies, C. Uihlein, and C. Schwab, Assignment of the Even-Parity Excitons in Cu$_2$O, Phys. Rev. Lett. **43**, 1260 (1979).

[11] C. Uihlein, D. Fröhlich, and R. Kenklies, Investigation of exciton fine structure in Cu$_2$O, Phys. Rev. B **23**, 2731 (1981).

[12] G. M. Kavoulakis, Y. Chang, and G. Baym, Fine structure of excitons in Cu$_2$O, Phys. Rev. B **55**, 7593 (1997).

[13] H. Matsumoto, K. Saito, M. Hasuo, S. Kono, and N. Nagasawa, Revived interest on yellow-exciton series in Cu$_2$O: An experimental aspect, Solid State Commun. **97**, 125 (1996).

[14] T. Kaczimierczuk, D. Fröhlich, S. Scheel, H. Stolz, and M. Bayer, Giant Rydberg excitons in the copper oxide Cu$_2$O, Nature (London) **514**, 343 (2014).

[15] M. Aßmann and M. Bayer, Semiconductor Rydberg physics, Adv. Quantum Technol. **3**, 1900134 (2020).

[16] J. Heckötter, D. Janas, R. Schwartz, M. Aßmann, and M. Bayer, Experimental limitation in extending the exciton series in Cu$_2$O towards higher principal quantum numbers, Phys. Rev. B **101**, 235207 (2020).

[17] M. A. M. Versteegh, S. Steinhauer, J. Bajo, T. Lettner, A. Soro, A. Romanova, S. Gyger, L. Schweickert, A. Mysyrowicz, and V. Zwiller, Giant Rydberg excitons in Cu$_2$O probed by photoluminescence excitation spectroscopy, Phys. Rev. B **104**, 245206 (2021).

[18] A. Browaeys and T. Lahaye, Many-body physics with individually controlled Rydberg atoms, Nat. Phys. **16**, 132 (2020).

[19] J. Heckötter, V. Walther, S. Scheel, M. Bayer, T. Pohl, and M. Aßmann, Asymmetric Rydberg blockade of giant excitons in cuprous oxide, Nat. Commun. **12**, 1 (2021).

[20] F. Schweiner, J. Main, M. Feldmaier, G. Wunner, and C. Uihlein, Impact of the valence band structure of Cu$_2$O on excitonic spectra, Phys. Rev. B **93**, 195203 (2016).

[21] F. Schöne, S.-O. Krüger, P. Grünwald, H. Stolz, S. Scheel, M. Aßmann, J. Heckötter, J. Thewes, D. Fröhlich, and M. Bayer, Deviations of the exciton level spectrum in Cu$_2$O from the hydrogen series, Phys. Rev. B **93**, 075203 (2016).

[22] J. Thewes, J. Heckötter, T. Kazimierczuk, M. Aßmann, D. Fröhlich, M. Bayer, M. A. Semina, and M. M. Glazov, Observation of High Angular Momentum Excitons in Cuprous Oxide, Phys. Rev. Lett. **115**, 027402 (2015).

[23] F. Schweiner, J. Main, G. Wunner, M. Freitag, J. Heckötter, Ch. Uihlein, M. Aßmann, D. Fröhlich, and M. Bayer, Magnetoexcitons in cuprous oxide, Phys. Rev. B **95**, 035202 (2017).

[24] M. Aßmann, J. Thewes, D. Fröhlich, and M. Bayer, Quantum chaos and breaking of all anti-unitary symmetries in Rydberg excitons, Nat. Mater. **15**, 741 (2016).

[25] P. Grünwald, M. Aßmann, J. Heckötter, D. Fröhlich, M. Bayer, H. Stolz, and S. Scheel, Signatures of Quantum Coherences in Rydberg Excitons, Phys. Rev. Lett. **117**, 133003 (2016).

[26] S. Zielińska-Raczyńska, G. Czajkowski, and D. Ziemkiewicz, Optical properties of Rydberg excitons and polaritons, Phys. Rev. B **93**, 075206 (2016).

[27] S. Zielińska-Raczyńska, D. Ziemkiewicz, and G. Czajkowski, Electro-optical properties of Rydberg excitons, Phys. Rev. B **94**, 045205 (2016).

[28] S. Zielińska-Raczyńska, D. Ziemkiewicz, and G. Czajkowski, Magneto-optical properties of Rydberg excitons: Center-of-mass quantization approach, Phys. Rev. B **95**, 075204 (2017).

[29] F. Schöne, H. Stolz, and N. Naka, Phonon-assisted absorption of excitons in Cu$_2$O, Phys. Rev. B **96**, 115207 (2017).

[30] D. Semkat, H. Fehske, and H. Stolz, Influence of electron-hole plasma on Rydberg excitons in cuprous oxide, Phys. Rev. B **100**, 155204 (2019).

[31] V. Walther and T. Pohl, Plasma-Enhanced Interaction and Optical Nonlinearities of Cu$_2$O Rydberg Excitons, Phys. Rev. Lett. **125**, 097401 (2020).

[32] A. Farenbruch, D. Fröhlich, D. R. Yakovlev, and M. Bayer, Rydberg Series of Dark Excitons in Cu$_2$O, Phys. Rev. Lett. **125**, 207402 (2020).

[33] J. Mund, D. Fröhlich, D. R. Yakovlev, and M. Bayer, High-resolution second harmonic generation spectroscopy with femtosecond laser pulses on excitons in Cu$_2$O, Phys. Rev. B **98**, 085203 (2018).

[34] J. P. Rogers, L. A. P. Gallagher, D. Pizzey, J. D. Pritchett, C. S. Adams, M. P. A. Jones, C. Hodges, W. Langbein, and S. A. Lynch, High-resolution nanosecond spectroscopy of even-parity Rydberg excitons in Cu$_2$O, Phys. Rev. B **105**, 115206 (2022).

[35] P. Rommel, J. Main, A. Farenbruch, J. Mund, D. Fröhlich, D. R. Yakovlev, M. Bayer, and Ch. Uihlein, Second harmonic generation of cuprous oxide in magnetic fields, Phys. Rev. B **101**, 115202 (2020).

[36] A. Farenbruch, J. Mund, D. Fröhlich, D. R. Yakovlev, M. Bayer, M. A. Semina, and M. M. Glazov, Magneto-Stark and Zeeman effect as origin of second harmonic generation of excitons in Cu$_2$O, Phys. Rev. B **101**, 115201 (2020).

[37] N. Naka and N. Nagasawa, Dynamics of paraexcitons generated in a 3D confined potential well by two-photon resonance excitation in Cu$_2$O, J. Lumin. **94**, 413 (2001).

[38] N. Naka and N. Nagasawa, Two-photon diagnostics of stress-induced exciton traps and loading of 1s-yellow excitons in Cu$_2$O, Phys. Rev. B **65**, 075209 (2002).

[39] A. Konzelmann, B. Frank, and H. Giessen, Quantum confined Rydberg excitons in reduced dimensions, J. Phys. B: At. Mol. Opt. Phys. **53**, 024001 (2020).

[40] S. Steinhauer, M. A. Versteegh, S. Gyger, A. W. Elshaari, B. Kunert, A. Mysyrowicz, and V. Zwiller, Rydberg excitons in Cu$_2$O microcrystals grown on a silicon platform, Commun. Mater. **1**, 1 (2020).

[41] A. M. Konzelmann, S. O. Krüger, and H. Giessen, Interaction of OAM light with Rydberg excitons: Modifying dipole selection rules, Phys. Rev. B **100**, 115308 (2019).

[42] S. O. Krüger, H. Stolz, and S. Scheel, Interaction of charged impurities and Rydberg excitons in cuprous oxide, Phys. Rev. B **101**, 235204 (2020).

[43] K. Orfanakis, S. K. Rajendran, V. Walther, T. Volz, T. Pohl, and H. Ohadi, Rydberg exciton-polaritons in a Cu$_2$O microcavity, Nat. Mater. **21**, 767 (2022).

[44] A. Mokhberi, M. Hennrich, and F. Schmidt-Kaler, Trapped Rydberg ions: A new platform for quantum information processing, Adv. At. Mol. Opt. Phys. **69**, 233 (2020).

[45] M. Okuda, K. Deguchi, A. Iwamae, H. Nakamura, K. Sawada, and M. Hasuo, Simulation of optical near field of a sub-wavelength gold slit array and its electric quadrupole interaction with 1s excitons in Cu$_2$O, Phys. Status Solidi C **3**, 3547 (2006).

[46] N. Yang and A. E. Cohen, Local geometry of electromagnetic fields and its role in molecular multipole transitions, J. Phys. Chem. B **115**, 5304 (2011).

[47] J. D. Jackson, *Classical Electrodynamics* (John Wiley & Sons, New York, 1962), p. 101.

[48] J. D. Jackson, *Classical Electrodynamics* (John Wiley & Sons, New York, 1962), p. 101, Eq. (4.17).

[49] C. T. Schmiegelow, J. Schulz, H. Kaufmann, T. Ruster, U. G. Poschinger, and F. Schmidt-Kaler, Transfer of optical orbital angular momentum to a bound electron, Nat. Commun. **7**, 1 (2016).

[50] S. Franke-Arnold, Optical angular momentum and atoms, Philos. Trans. R. Soc. A **375**, 20150435 (2017).

[51] V. E. Lembessis and M. Babiker, Enhanced Quadrupole Effects for Atoms in Optical Lattices, Phys. Rev. Lett. **110**, 083002 (2013).

[52] G. F. Quinteiro, F. Schmidt-Kaler, and C. T. Schmiegelow, Twisted-Light-Ion Interaction: The Role of Longitudinal Fields, Phys. Rev. Lett. **119**, 253203 (2017).

[53] F. Machado, N. Rivera, H. Buljan, M. Soljačić, and I. Kaminer, Shaping polaritons to reshape selection rules, ACS Photonics **5**, 3064 (2018).

[54] R. J. Elliott, Symmetry of excitons in Cu_2O, Phys. Rev. **124**, 340 (1961).

[55] G. F. Koster, J. O. Dimmock, R. Wheeler, and H. Statz, *Properties of the Thirty-Two Point Groups* (The MIT Press Research Monographs, Cambridge, 1963).

[56] T. Weiss, G. Granet, N. A. Gippius, S. G. Tikhodeev, and H. Giessen, Matched coordinates and adaptive spatial resolution in the Fourier modal method, Opt. Express **17**, 8051 (2009).

[57] T. Weiss, N. A. Gippius, S. G. Tikhodeev, G. Granet, and H. Giessen, Derivation of plasmonic resonances in the Fourier modal method with adaptive spatial resolution and matched coordinates, J. Opt. Soc. Am. A **28**, 238 (2011).

[58] D. Dregely, F. Neubrech, H. Duan, R. Vogelgesang, and H. Giessen, Vibrational near-field mapping of planar and buried three-dimensional plasmonic nanostructures, Nat. Commun. **4**, 2237 (2013).

[59] B. Metzger, M. Hentschel, T. Schumacher, M. Lippitz, X. Ye, Ch. B. Murray, B. Knabe, and H. Giessen, Doubling the efficiency of third harmonic generation by positioning ITO nanocrystals into the hot-spot of plasmonic gap-antennas, Nano Lett. **14**, 2867 (2014).

[60] M. Hentschel, Complex 2D & 3D Plasmonic Nanostructures Fano Resonances, Chirality, and Nonlinearities, Ph.D. thesis, University of Stuttgart, 2013.

[61] H. Stolz, R. Schwartz, J. Heckötter, M. Aßmann, D. Semkat, S.-O. Krüger, and M. Bayer, Coherent transfer matrix analysis of the transmission spectra of Rydberg excitons in cuprous oxide, Phys. Rev. B **104**, 035206 (2021).

[62] J. Heckötter, Strongly interacting Rydberg excitons in Cu_2O, Ph.D. thesis, Technical University Dortmund, 2020.

[63] J. Heckötter, M. Freitag, D. Fröhlich, M. Aßmann, M. Bayer, P. Grünwald, F. Schöne, D. Semkat, H. Stolz, and S. Scheel, Rydberg Excitons in the Presence of an Ultralow-Density Electron-Hole Plasma, Phys. Rev. Lett. **121**, 097401 (2018).

[64] H. Stolz and D. Semkat, Scattering of Rydberg excitons by phonon-plasmon modes, J. Phys.: Condens. Matter. **33**, 425701 (2021).